



Microstructure formation of Ti-6Al-4 V in synchronous induction assisted laser deposition



Wei Fan ¹, Hua Tan ^{*,1}, Xin Lin, Weidong Huang

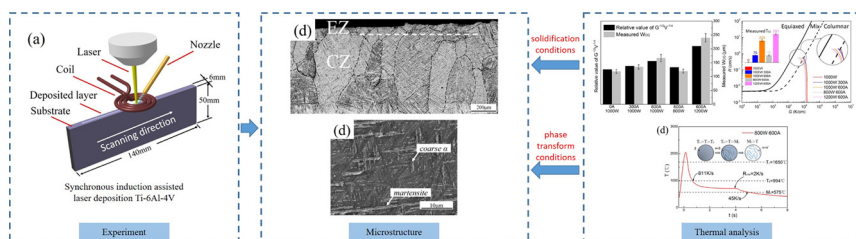
State Key Laboratory of Solidification Processing, Northwestern Polytechnical University, Xi'an, 710072, PR China

Key Laboratory of Metal High Performance Additive Manufacturing and Innovative Design, MIIT China, Northwestern Polytechnical University, Xi'an, 710072, PR China

HIGHLIGHTS

- Synchronous induction assisted laser deposition is proposed.
- A thermal analysis model of synchronous induction assisted laser deposition is established.
- Microstructural evolution mechanisms of synchronous induction assisted laser deposition are revealed.
- The grains and phase can potentially be controlled separately by synchronous induction assisted laser deposition process.

GRAPHICAL ABSTRACT



ARTICLE INFO

Article history:

Received 14 August 2018

Received in revised form 17 October 2018

Accepted 2 November 2018

Available online 4 November 2018

Keywords:

Synchronous induction assisted laser deposition

Ti-6Al-4 V alloy

Microstructure

Thermal behavior

Mathematical model analysis

ABSTRACT

Laser deposition (LD) is a useful repair technique and in-situ microstructure control is significant. However, the ability of in-situ microstructural control is inevitably limited in LD. Introducing induction heating into laser deposition is a potential solution for this challenging issue. In this research, the synchronous induction assisted laser deposition of Ti-6Al-4 V alloy were conducted and a thermal analysis model was established to investigate the influences of laser and induction energy on the morphology and size of the grains, the phase, and the Vickers hardness. Results showed that both of the thickness of equiaxed grain zone and the width of columnar grains increased with increasing laser energy and induction energy. The fraction of α phase increases with increasing induction energy due to sharply reduction of cooling rate during the cooling period caused by the post-heating, while the fraction of martensite increased with increasing laser energy. The “800 W-600A” and “1000 W-300A” samples have similar β grain morphology and size but consist of different phase, which is very distinctive from usual laser deposition process. This novel discovery indicates a great potential of microstructure control, the grains and the phase can be controlled separately by adjusting the laser parameters and induction parameters.

© 2018 Elsevier Ltd. This is an open access article under the CC BY-NC-ND license (<http://creativecommons.org/licenses/by-nc-nd/4.0/>).

1. Introduction

Laser deposition (LD) is one of the high-performance additive manufacturing technologies and has attracted much attention due to its immanent advantages [1,2]. LD provides a useful solution for the

low-cost repairing of damaged high value components in industry application field. In the repairing process, the metallic powder are projected onto the wrought or cast substrate and formed a deposited layer with melting and solidification, then the worn part can be repaired with multi-track and multi-layer depositions [3,4]. Unlike the laser deposited samples, the repairing of damaged components will consideration of the matching relationship between the mechanical properties of repaired zone and body part. The expectation of the mechanical properties of repaired zone varies with different substrate and the ability of

* Corresponding author.

E-mail address: tanhua@nwpu.edu.cn (H. Tan).

¹ These authors contributed equally to this work.

microstructural control is significant because the microstructure is the decisive factor for mechanical properties [5–7]. Meanwhile, in-situ microstructural control is more suitable than post heat treatment in order to remain the mechanical properties of the substrate. However, the effect of the temperature field control is inevitably limited since only single heat source is working. In addition, the serious stress would be caused due to high temperature gradient in LD process, even results in sample cracking.

In LD, in order to reduce the stress concentration and eliminate cracks, induction heating has been widely introduced as a preheating source because of its complementary characteristics with laser (low cost, large heating area, low energy density) [8–10]. So far, preheating the whole part before laser deposition has been a mostly used method of hybrid processing. However, the whole preheating means is lack of flexibility and only apply to small sample processing, and cannot satisfy the requirements of real-time and in-situ controlled temperature field in laser additive manufacturing of large part. F. Brückner [11] compared four typical kinds of hybrid method (whole part heating, inductive preheating, inductive post-heat treatment and their combined application with a ring coil) during LD process, and found that the temperature fields can be change flexibly by synchronous induction heating. Hence, considering multidirectional deposition requirement, synchronous induction heating with a moving coil around the laser beam has greater potential to achieve the flexible control of thermal behavior, microstructure and mechanical properties. However, further study on the microstructure evolution in synchronous induction assisted laser deposition is scarce.

Ti-6Al-4 V titanium alloy is widely used in the aerospace and is suitable for laser additive manufacturing technology. In this study, with introduction of synchronous induction, some Ti-6Al-4 V titanium depositions were carried out, the microstructure characteristic and thermal behavior were investigated, and the influence mechanism of the thermal behavior caused by two thermal heat source on microstructure formation were discussed.

2. Experimental procedure

Some single-pass deposition experiments were completed on the self-made synchronous induction assisted laser deposition system which is consisted of four subsystems: 3 kW fiber laser, 50 kW high frequency induction heater (15–35 kHz), powder feed system involve a side-injection nozzle tip and 3-axis working table. Fig. 1 shows the process of the synchronous induction assisted laser deposition. A plate 140 mm long, 6 mm wide, 50 mm high serves as the substrate, laser and inductive coil were set coaxially and heat the surface of substrate synchronously in the deposition experiment shown in Fig. 1(a). Fig. 1(b) presents more details about the formation of deposited layer, the laser beam and the coil keep stationary while the substrate moving with the working table and the powder flow from the side-injection nozzle was injected into the molten pool formed by the heating of the

two heat sources. The coil with an inner diameter of 10 mm and an outer diameter of 25 mm was placed about 2 mm from the surface of the substrate and parallel to it during the whole deposition process. The triple helix coil was coiled by a copper tube with a diameter of 5 mm.

In this study, commercially Ti-6Al-4 V powder with particles size range of 45–80 μm was dried for 4 h in a vacuum drying furnace at 400 K before the experiment to remove the absorbed water. The average chemical composition (wt%) of the powder was measured as Al-6.15, V-4.00, Fe-0.30, C-0.10, N-0.05, H-0.015, O-0.20 and Ti-balance. The substrate was a Ti-6Al-4 V plate with the same chemical composition of the powder and had been sanding and washed by acetone prior to deposition. A series of single tracks with a length of 80 mm were deposited using the synchronous induction assisted laser deposition system in an inert atmosphere (argon gas) environment with the oxygen content was controlled under 100 ppm. The processing parameters are shown in Table 1 and the process variables include laser power and input current of induction heating. Those single tracks were cut along the longitudinal section and the metallographic specimens were made. Subsequently, all the specimens were prepared using a standard mechanical polishing means and etched by the Kroll etching agent. The macrostructure was observed by an OLYMPUS optical microscope (OM) and microstructure was examined using a Hitachi S-4800 scanning electron microscope (SEM). The microhardness in the deposited layer was measured using a Struers Duramin-A300 microhardness tester.

3. Results

3.1. Grain morphology

Fig. 2 shows the longitudinal section of the tracks deposited under the processing parameters detailed in Table 1 and the deposited layer was distinguished into two zones by the morphologies of grains. The columnar grains growing epitaxially from substrate formed the columnar grains zone (CZ) and the equiaxed grains in the top region of the deposited layers were defined as the equiaxed grains zone (EZ). It can be noticed that the depth of melt pool, the width of columnar grain and the thickness of equiaxed grains zone varies significantly with different input current and laser power.

Fig. 2(a)–(c) present the influence of induction energy on the morphologies of grains. There is no EZ in the 1000 W-0A sample (Fig. 2(a)), all the deposited layer are composed of columnar grains. With the addition of synchronous induction heating, equiaxed grains can be observed at the top region in 1000 W-300A and 1000 W-600A samples. When the input current increased from 0A to 600A, the thickness of EZ (T_{EZ}) increased from 0 μm to 75 μm , then to 225 μm . Meanwhile the average width of columnar grains increased markedly (from 119 μm to 167 μm) with the increase of induction energy. Fig. 2(c)–(e) clearly show the influence of laser energy on the morphologies of grains. The thickness of EZ increases from 75 μm to 293 μm and the average

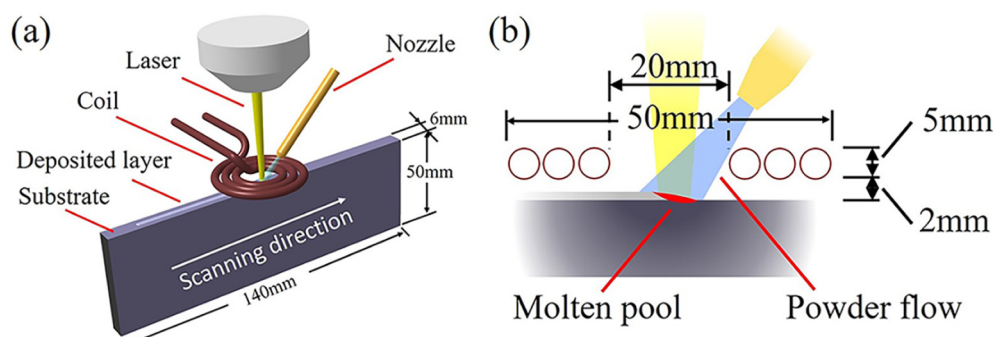


Fig. 1. Synchronous induction assisted laser deposition process: (a) schematic diagram, (b) detail drawing.

Table 1

Processing parameters of synchronous induction assisted laser deposition experiment.

Laser power	Current intensity	Scanning velocity	Feed rate of powder	voltage	Beam diameter
1000 W	0A	6 mm/s	12 g/min	550 V	3 mm
1000 W	300A				
1000 W	600A				
800 W	600A				
1200 W	600A				

width of columnar grains increases from 120 μm to 240 μm as the laser power increases from 800 W to 1200 W. Comparing the influence law of these two heat source, it can be found the thickness of EZ is both closely related to the laser and induction energy but the laser energy exhibit superior influence on the average width of columnar grains than the induction energy. Furthermore, it should be noticed that both the thickness of EZ and the average width of columnar grains are very close in the 1000 W-300A and 800 W-600A samples. It implies that the synergetic controlling of the laser and induction energy can effectively adjust solidification condition in LD.

3.2. Phase

Fig. 3 demonstrates the microstructure in the prior β grains at the middle of the deposited layer and the extracted fraction of α phase in five samples. As indicated in Fig. 3(a), the 1000 W-0A sample is composed of vertical martensites and β phase which is consistent with the observation from the single track deposition by LSF. As shown in Fig. 3(b), the microstructure in 1000 W-300A sample is mainly martensites and a very small amount of α phase precipitate from the β grain, the morphology of α phase can be hardly distinguished. However, several morphologies of α phase can be observed in the 1000 W-600A, 800 W-600A and 1200 W-600A samples, as indicated in Fig. 3(c)–(e). Compared the microstructure in Fig. 3(a)–(c), it can be found that the acicular martensite convert to lath martensite when the input current increases from 0A to 300A, and the fraction of α phase increases meanwhile. When the input current rose to 600A, the microstructure in single track transformed obviously, α laths and acicular α can be observed, but the size of martensites has not changed. The martensites keep $40 \pm 36 \mu\text{m}$ for length and $1.1 \pm 0.6 \mu\text{m}$ for width when the input current increases. On the contrary, when laser power increases from 800 W to 1200 W, the microstructure transforms from mainly α phase to mainly α' phase, as shown in Fig. 3(c), (d) and (e). In the 800 W-600A sample, a small number of martensite phase can be observed, α phase distribute as the classical ‘basket-weave’ Widmanstätten morphology. When laser power rises to 1000 W, the fraction of martensite increases and the fraction of α decreases, and the morphology of α phase transforms to lathy and acicular from ‘basket-weave’. The contents of martensites keep increasing with laser power increases to 1200 W, and the morphology of α phase transforms to irregular acicular shape. With the increasing of laser energy, the width of α laths reduced from $1.1 \pm 0.3 \mu\text{m}$ to $0.4 \pm 0.1 \mu\text{m}$ and the width of martensites decreased from $1.5 \pm 0.4 \mu\text{m}$ to $1 \pm 0.8 \mu\text{m}$. Fig. 3(f) displays the fraction of α phase extracted from the SEM picture of the five samples. It can be seen that the fraction of α phase increases from 0% to 67.8% with the increase of input current and decreases from 82.5% to 26.4% with the increase of laser power.

X-ray diffraction (XRD) profiles in Fig. 4 further verify the phase constitution in each samples. Fig. 4(a) shows that all the samples are consist of $\alpha + \alpha'$ and β phase. It should be noticed that both of α phase and α' have hexagonally close-packed crystal structure and their lattice parameters are close, so it is difficult to distinguish them from Fig. 4(a). The angle of diffraction peak is usually used to reveal the lattice unit cell of $\alpha + \alpha'$ phase and estimate the fraction of each phases qualitatively [12]. Fig. 4(b) shows the enlarged XRD profiles, it can be seen

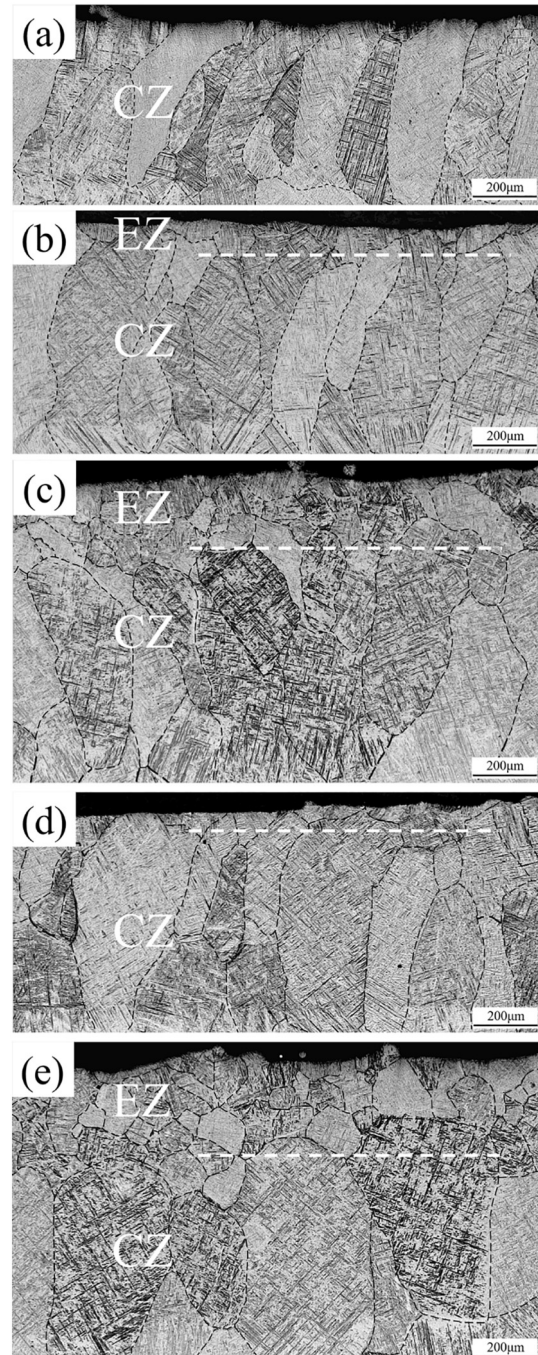


Fig. 2. The morphologies of grains under OM and the deposited layer are divided into equiaxed grain zone (EZ) and columnar grain zone (CZ): (a) 1000 W power and 0A current, (b) 1000 W power and 300A current, (c) 1000 W power and 600A current, (d) 800 W power and 600A current, (e) 1200 W power and 600A current.

that angle of (001) diffraction peak becomes larger with the increasing input current and reduces with the increasing laser power. Jingjing Yang [13] had measured the lattice constant of α phase (a is $2.9235 \pm 0.0012 \text{ \AA}$ and c is $4.6593 \pm 0.0020 \text{ \AA}$) and α' phase (a is $2.9381 \pm 0.0016 \text{ \AA}$ and c is $4.6684 \pm 0.0014 \text{ \AA}$), so the reduce of the angle of diffraction peak means the increases of lattice constant a and the decrease of the fraction of α phase. So Fig. 4(b) demonstrates that the fraction of α phase have not significant changes when input current increases to 300A from 0A and have a big increase when input current rise to 600A. Meanwhile, the fraction of α phase reduces with the laser power increases from 800 W to 1200 W. The result of XRD profiles is consistent with the

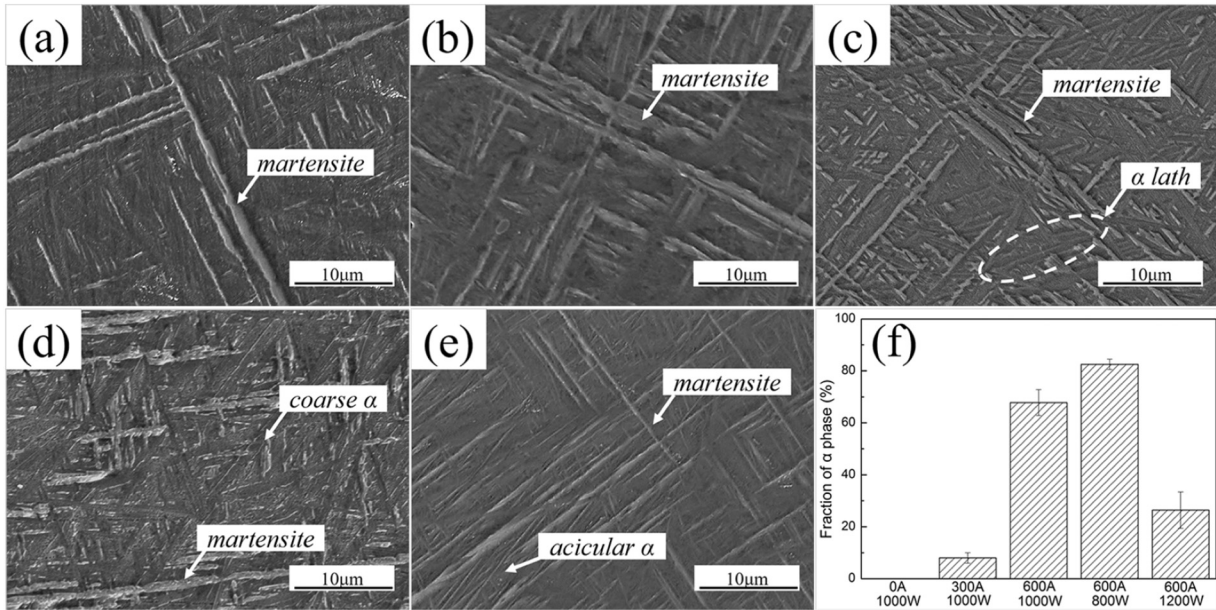


Fig. 3. The phase inside β grains: (a) 1000 W power and 0A current, (b) 1000 W power and 300A current, (c) 1000 W power and 600A current, (d) 800 W power and 600A current, (e) 1200 W power and 600A current, (f) fraction of α phase in each samples.

observation from scanning electron microscopy (SEM) images which had displayed in the Fig. 3(f).

3.3. Microhardness measurements

Fig. 5 shows the average Vickers hardness of the samples under different processing parameters. With the increase of input current from 0A to 300A, the average hardness only has a slightly fall from 416.6 HV to 415 HV. However, as the input current continues to rise to 600A, the average hardness decreases from 415 HV to 375.8 HV. The influence of induction energy on hardness shows an exponential decline. With the increase of laser power, the average hardness increases in a linear pattern, i.e. from 368.3 HV (800 W-600A) to 375.8 HV (1000 W-600A) and then to 385.8 HV (1200 W-600A).

The deformation patterns around the micro-hardness indentations could also be used to analyze the elastoplastic behavior of the materials fabricated in small size [14–16]. Fig. 6 displays the optic microstructure images which were taken around the Vickers indentations of the synchronous induction assisted laser deposition samples. Two types of slip bands can be found around the indentations which are usually

seen: straight slip band and wavy slip band. The wavy slip bands mean a larger plastic deformation than the straight slip bands in a material [14]. Straight slip bands are found in the optical micrograph presented in Fig. 6(a) and (b) for 1000 W-0A and 1000 W-300A samples and wavy slip bands which are irregular and semi-circular bands can be observed in the 1000 W-600A sample in Fig. 6(c). From Fig. 6(c–e), it can be found that the bands transform to straight type from wavy type when the laser power increases to 1200 W from 800 W. Therefore, the 800 W-600A and 1000 W-600A samples exhibit lower plasticity compared to the else samples.

4. Discussions

4.1. Thermal analysis

In additive manufacturing, the shape of molten pool and the evolution of solidification conditions are very hard to obtain by experimental measurement. In this case, the numerical simulation of temperature field has been widely applied to analyze the distribution of stress and explain the change of microstructure [3,7,8]. A mathematical thermal

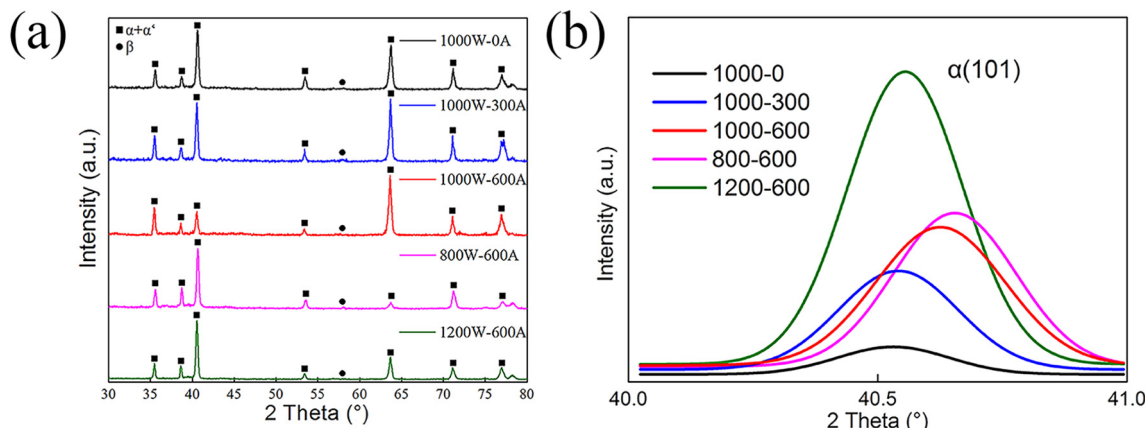


Fig. 4. XRD results of the samples deposited by synchronous induction assisted laser deposition under different processing parameters: (a) XRD profiles; (b) enlarged profiles of $\alpha(001)$ peak. The peak position shift takes place due to the changes in composition of each phase.

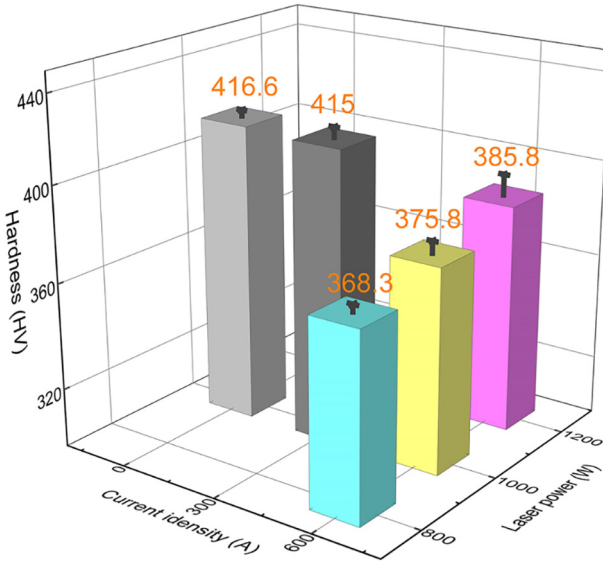


Fig. 5. Vickers hardness of synchronous induction assisted laser deposition Ti-6Al-4 V alloy.

analysis model of the synchronous induction assisted laser deposition is established here and the temperature at any point $T(x, y, z)$ can be seen as the sum of the temperature field caused by induction heating ($T_I(x, y, z)$) and laser ($T_L(x, y, z)$)

$$T(x, y, z) = T_L(x, y, z) + T_I(x, y, z) + T_0 \quad (1)$$

where T_0 is the initial temperature of the substrate.

In this model, both the laser and induction heating are treated as the surface heat source with a uniform heat intensity distribution. According to the solution developed by Rosenthal and Rykalin [17] for an infinite thin plate, $T_L(x, y, z)$ and $T_I(x, y, z)$ can be expressed as the quasi-steady state solution of a moving point heat source for a three-dimensional conduction

$$T_L(x, y, z) = \iint \frac{Q_L}{2\pi\lambda R} \exp\left(-\frac{v(x-x_0)}{2\alpha}\right) \exp\left(-\frac{vR}{2\alpha}\right) dS_L \quad (2)$$

$$T_I(x, y, z) = \iint \frac{Q_I}{2\pi\lambda R} \exp\left(-\frac{v(x-x_0)}{2\alpha}\right) \exp\left(-\frac{vR}{2\alpha}\right) dS_I \quad (3)$$

where $R^2 = (x-x_0)^2 + (y-y_0)^2 + (z-z_0)^2$, (x_0, y_0, z_0) are the coordinates of the point in the moving coordinate system, Q_L and Q_I are the heat intensity of laser and induction heating respectively, v is the scanning velocity, λ stands for the thermal diffusivity and α is the thermal conductivity, S_L and S_I are the position of heating zone of laser and induction heating.

As Eqs. (2) and (3) are workable only for a semi-infinite substrate, an approximate treatment mean is introduced in this model to transform the thin wall substrate into a semi-infinite space [18]. Two image heat sources of laser are added shown in Fig. 7 corresponding to the two side boundary of the substrate. The image heat sources have the same x value with the actual heat source. In the y direction, the difference between the two imaged laser and the real laser is equal to the width of the substrate.

Then the $T_L(x, y, z)$ can be expressed as

$$T_L(x, y, z) = \sum_{n=-1}^{n=1} \int_{-\frac{R}{2}}^{\frac{R}{2}} \int_{-\sqrt{\frac{R^2}{4}-x_0^2+nW}}^{\sqrt{\frac{R^2}{4}-x_0^2+nW}} \frac{Q_L}{2\pi\lambda R} \exp\left(-\frac{v(x-x_0)}{2\alpha}\right) \exp\left(-\frac{vR}{2\alpha}\right) dy_0 dx_0 \quad (4)$$

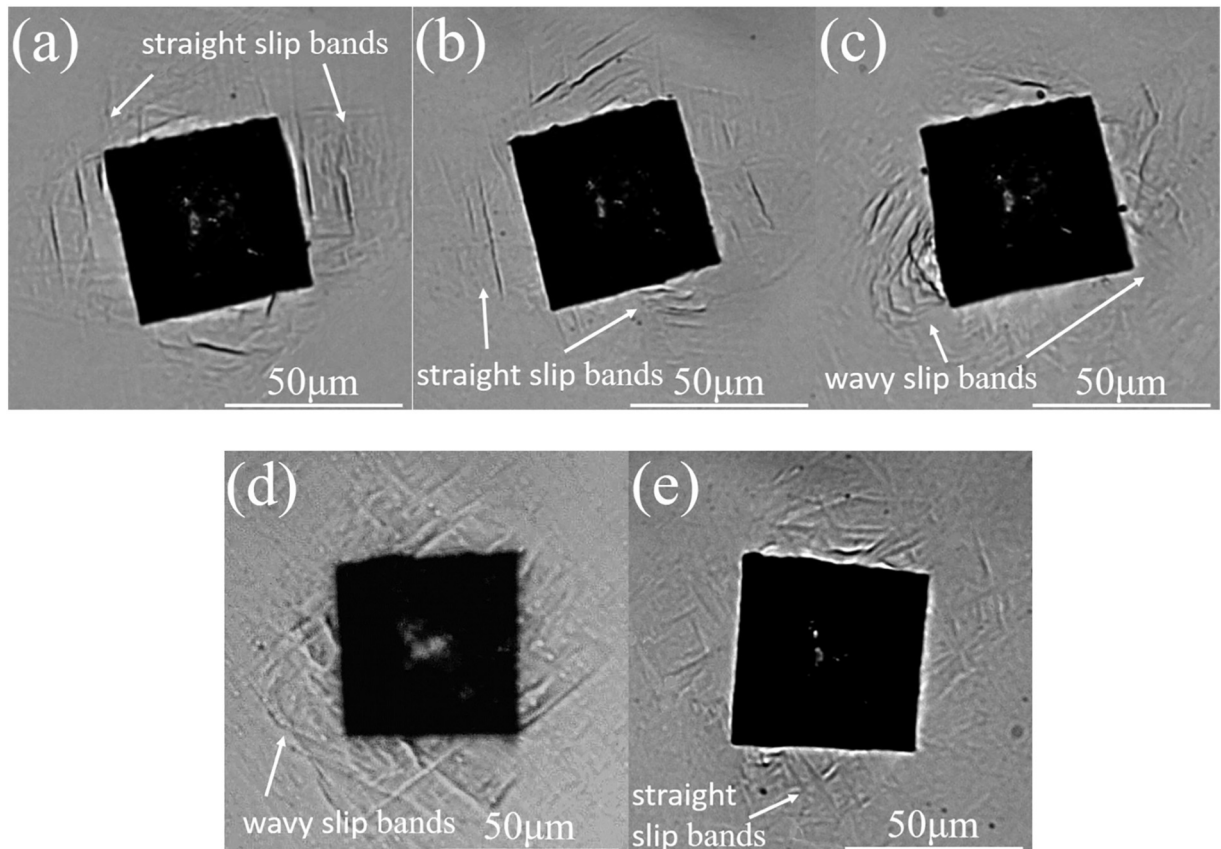


Fig. 6. The optical microstructures around the Vickers indentation taken for the synchronous induction assisted laser deposition samples: (a) 1000 W power and 0 A current, (b) 1000 W power and 300 A current, (c) 1000 W power and 600 A current, (d) 800 W power and 600 A current, (e) 1200 W power and 600 A current.

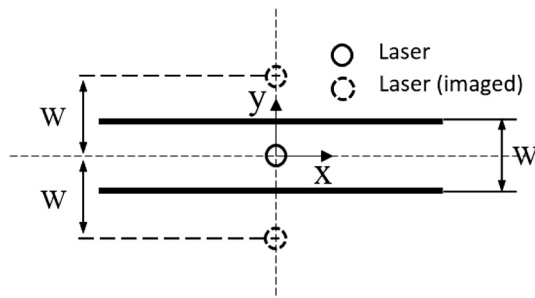


Fig. 7. Schematic diagram of the heat flow model formulation for laser.

where W is the width of the substrate, D is the diameter of laser beam. The heat intensity of laser is described by

$$Q_L = \frac{4P\beta}{\pi D^2} \quad (5)$$

where P is the laser power and β is the laser absorptivity.

The Q_I in $T_I(x, y, z)$ are influenced by many factors and there is no universal expression for calculating, compared with Q_L . Hence two temperature distributions are contrasted to obtain the value of Q_I , one is calculated by a transient thermal analysis model [17] and another is achieved by infrared measuring experiment. Fig. 8 shows the temperature distribution in static induction heating process at different time measured by an infrared thermometer. The structural dimension parameters of static induction heating experiment were set in concordance with the deposition experiment and the input current of induction heating is 600A. The figure displays the infrared temperature images at 2 s, 4 s, 6 s, 8 s and the temperatures of 7 points equidistantly distributed along the center line of the substrate are extracted. It can be seen that the temperature of substrate keep constant within 5 mm distance of the coil and then drops slowly close to the center, finally reaching the minimum at the center. Based on the measured distribution of temperature field, Fig. 9 shows the defined S_I in Eq. (3). The S_I is divided into two symmetrical parts and the inductive heat source heat up the area within the range of R_2 to R_1 in x direction for each one. And in the positive and negative direction of y -axis, S_I is extended to infinity follow the “image source” method. So the transient thermal analysis model of induction heating can be expressed as

$$T_I(x, y, z, t) = \int_0^t \int_{-\infty}^{\infty} \left(\int_{R_2}^{R_1} \frac{2Q_I}{\rho C(4\pi\alpha\tau)^{3/2}} \exp\left(-\frac{R^2}{4\alpha\tau}\right) dx_0 \right. \\ \left. + \int_{-R_1}^{-R_2} \frac{2Q_I}{\rho C(4\pi\alpha\tau)^{3/2}} \exp\left(-\frac{R^2}{4\alpha\tau}\right) dx_0 \right) dy_0 d\tau \quad (6)$$

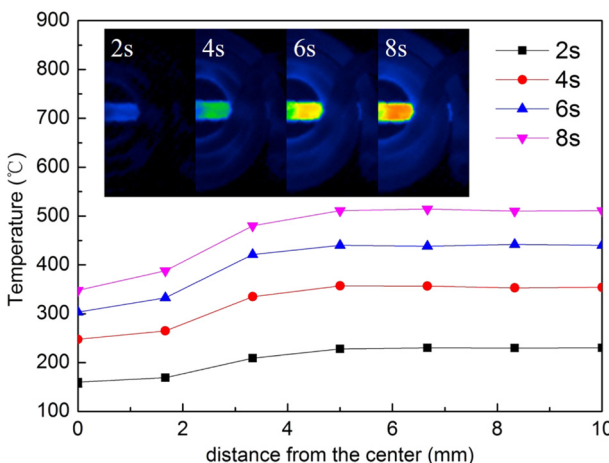


Fig. 8. Temperature distribution of static induction heating experiment.

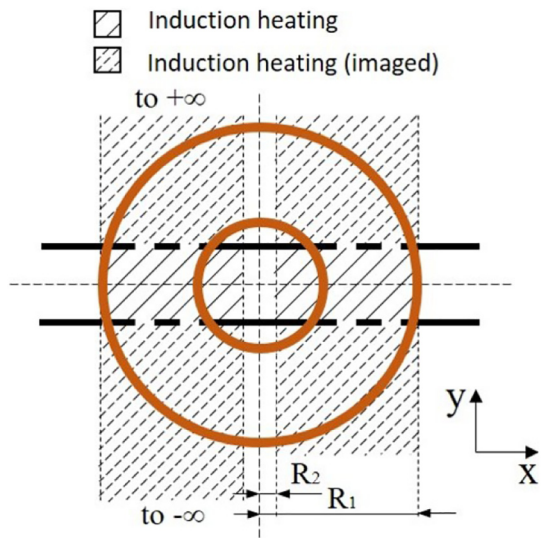


Fig. 9. Schematic diagram of the heat flow model formulation for induction heating.

where R_1 is the outer diameter of the coil and R_2 is an unknown value need to reverse seeking, ρ is the density of material, C is the specific heat capacity.

Take the measured temperature distribution at 2 s shown in Fig. 8 into the Eq. (6), then we get that $Q_I|_{I=600A}$ is 1.1 W/mm^2 and R_2 is 1 mm. Depending on the values, Fig. 10 displays the calculated and measured thermal behavior of point A (the center), point B (4 mm from the center), point C (8 mm from the center) and we can found that they are well matched. According to the value of $Q_I|_{I=600A}$, the value of $Q_I|_{I=300A}$ can be get by the relationship between heat intensity of induction heating Q_I and input current intensity I [19].

$$Q_I = K_0 I^2 \sqrt{\rho \mu f} \quad (7)$$

where K_0 is a coefficient depend on the structural dimensional parameters of the coil and the geometric parameters of the substrate, ρ is the electrical resistivity, μ is the magnetic conductivity and f is the frequency of input current.

The K_0 , ρ , μ and f are constant in the experiments and the Q_I is proportional to I^2 . So the $Q_I|_{I=300A}$ is a quarter of $Q_I|_{I=600A}$.

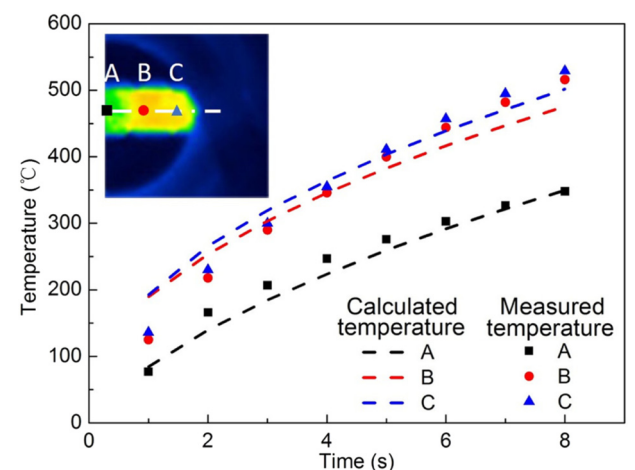


Fig. 10. Comparison diagram of calculated and measured temperature.

Based on the S_l defined in Fig. 9 the Eq. (3) can be developed as

$$T_l(x, y, z) = \int_{-\infty}^{\infty} \left(\int_{R_2}^{R_1} \frac{Q_l}{2\pi\lambda R} \exp\left(-\frac{v(x-x_0)+vR}{2\alpha}\right) dx_0 \right. \\ \left. + \int_{-R_1}^{-R_2} \frac{Q_l}{2\pi\lambda R} \exp\left(-\frac{v(x-x_0)+vR}{2\alpha}\right) dx_0 \right) dy_0 \quad (8)$$

According to Eqs. (1), (4), (8), the thermal analysis model of synchronous induction assisted laser deposition is established. The processing parameters and structural dimension parameters used in the experiment had been mentioned above and the thermophysical properties of Ti-6Al-4 V titanium alloy used in the calculation were shown in Table 2.

4.2. Effects of laser and induction energy on grain morphology

In laser deposition, the mechanical properties of fabricated parts are closely related to the grain morphology and size [22], while both of them are depend on the temperature gradient G and solidification rate R in front of solid-liquid interface [23,24]. Based on the thermal analysis model of synchronous induction assisted laser deposition, Fig. 11 shows the calculated solidification conditions in molten pool with the processing parameters in Table 1 and the critical condition of columnar to equiaxed transition (CET) of Ti-6Al-4 V alloy used here is developed by Hunt [25]. In Fig. 11, the lines represent the calculated solidification conditions of different parameters from the bottom to the top of the solid/liquid interface in the molten pool and the histogram displays the thicknesses of EZ which are extracted from Fig. 2. It can be seen from Fig. 11 that the differences in the solidification rates of five deposition parameters are not as significant as temperature gradient. When input energy increases (involve laser and induction heating), the maximum solidification rate has not a clear change. The influences of laser and induction heating on the temperature gradient are similar, the temperature gradient at the top of molten pool decreases with the increasing input energy. Even so, the temperature gradient shows stronger correlation with the input laser energy than induction heating, due to the higher energy intensity of laser heat source.

From Fig. 11, it can be seen that each of the solidification curves are mainly located in columnar grain zone and only a little part stretch into the mix zone, the insertion length of different parameters are enlarged. The top of lines mark the end of the solidification and the intersection points of solidification curves and CET curve means the beginning of equiaxed grain growth. It indicates that columnar grains take over most of middle and bottom of the molten pool and trend to equiaxed in the top. The length of the solidification curve stretched into mix grain zone can reflect the thickness of equiaxed grains in the deposited layer. In Fig. 11, the insertion length of solidification curves increase with the increase of laser power and input current. The solidification curve of 1200 W-600A sample has the longest insertion length and the 1000 W-0A sample has hardly any insertion length. It should be noticed that the insertion length of 1000 W-300A curve and 800 W-600A curve are almost the same. Compare the insertion length of solidification curves and the measured thickness of EZ, It can be found that there is a good agreement between the insertion length of solidification

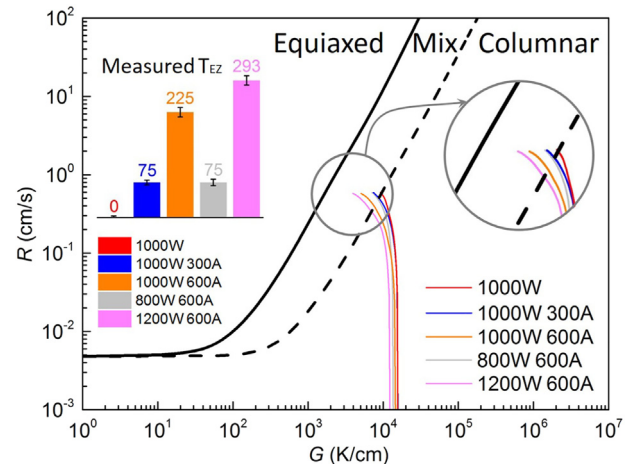


Fig. 11. Microstructure selection map of Ti-6Al-4 V alloy. The lines present the calculated solidification condition and the histogram shows the measured value of thickness of EZ (T_{EZ}).

curves and the measured value of thickness of EZ which displayed in the histogram of Fig. 11.

The width of columnar grains (W_{CG}) can be characterized by the primary dendrite arm spacing λ which is also related with the solidification rate R and temperature gradient G , the relationship can be expressed as [26].

$$\lambda = aG^{-1/2}V^{-1/4} \quad (9)$$

where a is a coefficient related to material properties.

In order to unify the solidification with different processing parameters, the average solidification condition from the bottom to the top of the solid/liquid interface in the molten pool was calculated by the formula as follow

$$G_z = \frac{1}{|z_{min}|} \int_{z_{min}}^0 G dz \quad (10)$$

$$R_z = \frac{1}{|z_{min}|} \int_{z_{min}}^0 R dz \quad (11)$$

Both of the average temperature gradient and solidification velocity in the depth direction are obtained by integral and the values are substituted into eq. (9). Fig. 12 shows the relative value of $G^{-1/2}V^{-1/4}$ and the width of columnar grains measured before. It can be found that the relative value of $G^{-1/2}V^{-1/4}$ increases with the increase of laser power and input current. The influences of input energy on the relative value of $G^{-1/2}V^{-1/4}$ tend to an exponential growth for laser power and a linear growth for input current. It can be found that the relative value of $G^{-1/2}V^{-1/4}$ of 800 W-600A sample and 1000 W-300A sample are almost equivalent.

4.3. Effects of laser and induction energy on phase

The thermal behavior curves of different processing parameters which belong to the center of molten pool are shown in Fig. 13, in order to investigate the formation mechanism of phase. When $t = 0$ s, the center of laser beam is overlap with the calculated point, then the powders and substrate suffered melting and solidification over time. It should be noticed that the curves only displayed the laser heating and inductive post-heating period because of the phase was determined by the thermal behavior after solidification. In Fig. 13, the cooling rate at β - α transus temperature T_β (994 °C) [27] and martensite starting temperature M_s (575 °C) [27] of Ti-6Al-4 V alloy have been identified.

Table 2

The thermophysical properties of Ti-6Al-4 V alloy used for calculation.

Parameters	Symbol	Value
Laser absorptivity (%)	β	34 [20]
Density (g/cm ³)	ρ	4.267 (1373 K) [21]
Thermal diffusivity (mm ² /s)	α	5.28 (1373 K) [21]
Heat capacity (J/kg·°C)	c	641 (1373 K) [21]
Thermal conductivity (W/m·K)	λ	19.3 (1373 K) [21]

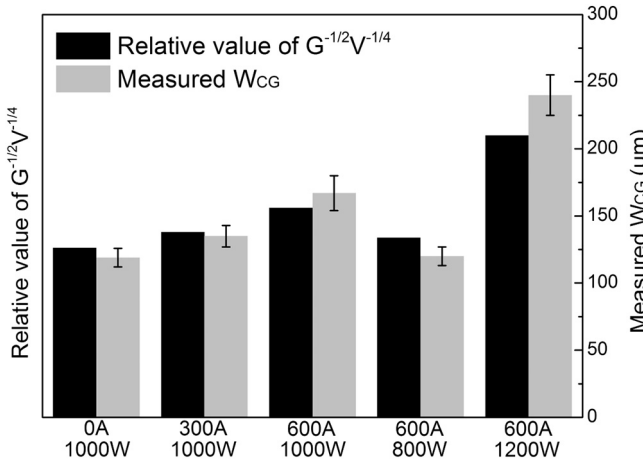


Fig. 12. Comparison diagram of relative value of $G^{-1/2} V^{1/4}$ and the measured width of columnar grains.

The schematic diagrams of the evolution of phase based on the thermal curves have been displayed when the molten metal cool down from liquid.

Compared the thermal behavior curves in Fig. 13(a–c), it can be found that the ambient temperature of substrate increases with the increasing input current due to the inductive pre-heating effect. With the input current rise to 600A from 0A, the ambient temperature of substrate rise to 450 °C from 20 °C. Meanwhile, the cooling rate reduce when input current rise to 600A from 0A due to the post-heating effect caused by the part of the coil which behind the laser in the scanning direction. The reduction of cooling rate at T_B is not significantly (1113 K/s to 1100 K/s) when the input current increase from 0A to 300A, but the cooling rate at M_S decrease from 256 K/s to 171 K/s. When the current rise to 600A, the cooling rate at T_B falls seriously from 1100 K/s to 437 K/s and the cooling rate at M_S decrease from 171 K/s to 81 K/s. Meanwhile, the shape of thermal behavior curve changed obviously. A “stair” appeared between T_B and M_S , and the slope becomes gently when the temperature drop below T_B and then back to steep when the temperature is close to M_S . The temperature of deposited layer reduced slowly on the “stair” and the cooling rate reaches minimum 3 K/s at the end of the “stair”. With the same input current (600A), Fig. 13(c–e) indicated the influence of laser power on the thermal behavior in synchronous induction assisted laser deposition. It can be seen that the ambient temperature of substrate are basically the same with the same input current, the maximal temperature of curves risen sharply with the increase of laser power. When laser power increases from 800 W to 1200 W, the cooling rate at T_B decreases sharply from 811 K/s to 305 K/s and that at M_S increases from 45 K/s to 100 K/s. The specific focus is the slope of the “stair” changed obviously. When laser power fall to 800 W from 1200 W, the “stair” becomes gentler and the minimum cooling rate decreases from 9 K/s to 2 K/s.

T. Ahmed summarized the phase transition of Ti-6Al-4 V alloy in the cooling process and gave the critical value of the cooling rate for different phase transitions [27]. The phase formations of Ti-6Al-4 V alloy in synchronous induction assisted laser deposition are displayed in Fig. 13 were obtained according to the calculated thermal curve based on his conclusion. The 1000 W-0A sample cools quickly from T_B to M_S and α phase is difficult to precipitate at this period, but when the temperature cool down under M_S the high cooling rate make the martensite precipitated rapidly. The 1000 W-300A sample experienced the similar thermal behavior with the 1000 W-0A sample, both of them are composed of martensite as shown in Fig. 3(a)(b). In the 1000 W-600A sample, α phase can be precipitated owing to the tiny cooling rate between T_B and M_S , but the hold time of low cooling rate is too short to complete the β - α transition. So there is still a fraction of martensite

can be transformed from the residual β phase like Fig. 13(c). Compare the thermal behavior curve in Fig. 13(c–e), it can be found that with the increase of laser power, the “stair” becomes shorter and steeper, it means the thermal conditions changed to be adverse to the precipitate of α phase. So the fraction of α phase decreases and the fraction of martensite increases with the increasing laser power which can well elucidate the evolution of phase shown in Fig. 3(c–e).

The analysis results of evolution of phase come to the same conclusion with the influence of laser power and input current on the hardness in Fig. 5. In titanium alloys, martensite phase has higher dislocation density than α phase and β phase and more hard than them because of dislocation strengthening. The hardness of 1000 W-0A sample is almost equivalent with the 1000 W-300A sample due to the same phase structures. And the hardness of 1000 W-600A sample drop sharply with the precipitate of α phase shown in Fig. 13(c). According to the evolution of phase shown in Fig. 13(c–e), the fraction of α phase decreases and the fraction of martensite increases with the increase of laser power, the hardness of deposited layer keep increasing when laser power rise to 1200 W from 800 W.

4.4. Microstructure control

In traditional laser additive manufacture technologies, the solidification conditions (temperature gradient and solidification velocity in front of solid/liquid interface) and the phase transformation condition (cooling rate) are closely related to input energy. Frederick [28] summarized the relationship between the input energy and solidification conditions

$$G = \frac{453.02}{E_d^{0.582}} \quad (12)$$

$$R = v \cos \left(\frac{81.15}{E_d^{0.05}} \right) \quad (13)$$

where $E_d = \frac{BP}{Vd}$, B is the bulk absorption coefficient, P is laser power, V is scanning velocity and d is the diameter of laser beam.

Meanwhile, the cooling rate can be expressed as

$$R_{cooling} = \frac{\partial T(x, y, z, t)}{\partial t} \quad (14)$$

And according to the transient thermal model of moving spot heat source [17].

$$T(x, y, z, t) = \frac{2Q}{\rho C(4\pi\alpha)^{3/2}} \exp\left(-\frac{vx}{2\alpha t}\right) \int_0^t \frac{1}{\tau^{3/2}} \exp\left(-\frac{v^2\tau}{4\alpha} - \frac{R^2}{4\alpha\tau}\right) d\tau \quad (15)$$

where Q had been defined in Eq. (5). The cooling rate can be written as

$$R_{cooling} = \frac{2Q}{\rho C(4\pi\alpha)^{3/2} t^{3/2}} \exp\left(\frac{-2vx - v^2 t}{4\alpha}\right) \exp\left(-\frac{R^2}{4\alpha t}\right) \quad (16)$$

From the Eqs. (12), (13) and (16), it can be found that temperature gradient, solidification velocity and cooling rate are the functions of laser power. The variations of laser power will cause the changes of temperature gradient, solidification velocity and cooling rate simultaneously. The result can be obtained that the change of grains and the evolution of phase are related, it is hardly to obtain the same grain with different phase and vice versa. This conclusion is consistent with the observation from Xinhua Wu [29], the increasing of laser power contributed to more thick grains and coarser α and β laths at the same time. Hence, the ability of microstructure control in laser additive

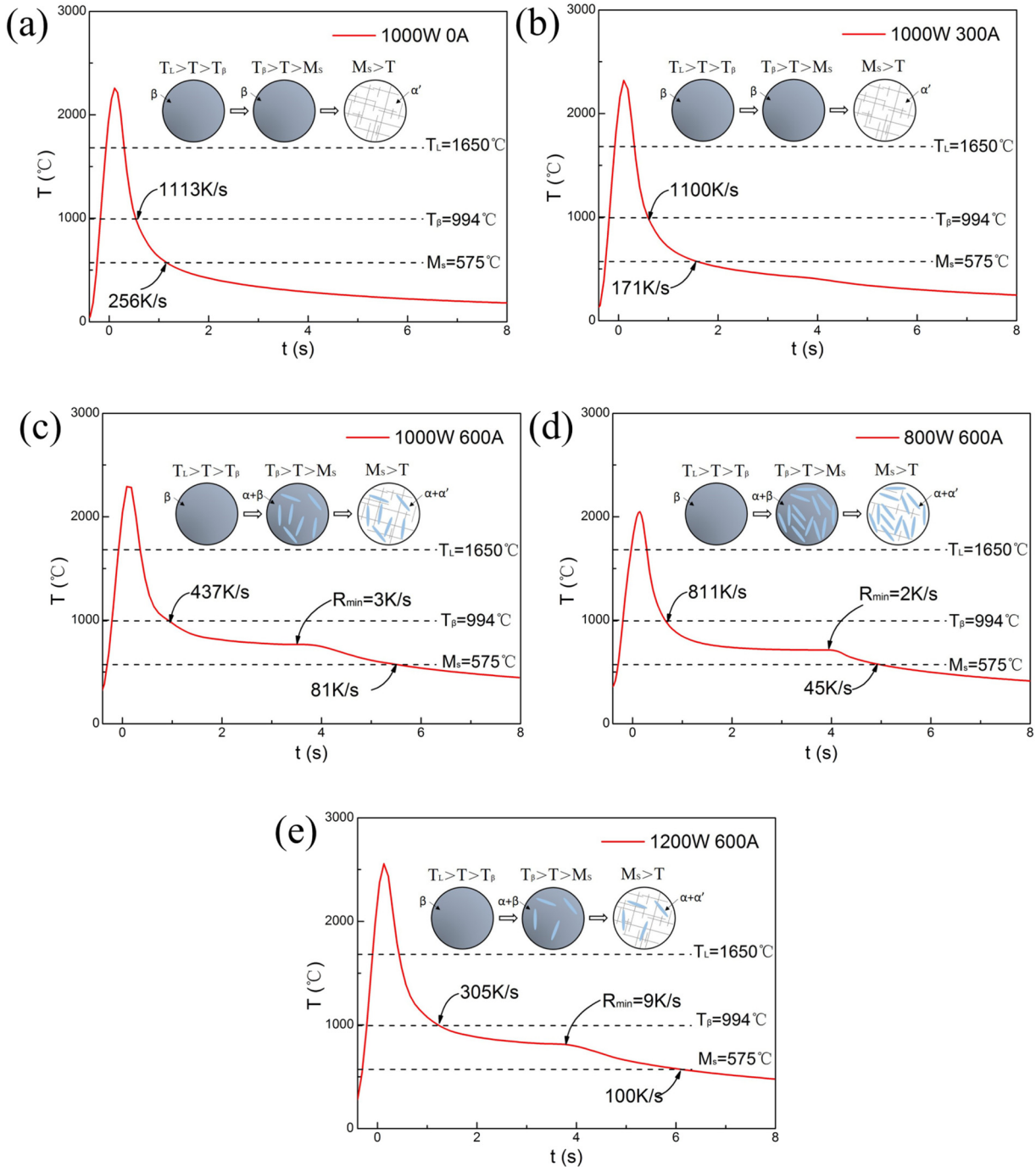


Fig. 13. Thermal behavior curve and the formation of phase for Ti-6Al-4V at the center of molten pool: (a) 1000 W power and 0A current, (b) 1000 W power and 300A current, (c) 1000 W power and 600A current, (d) 800 W power and 600A current, (e) 1200 W power and 600A current.

manufacturing is inevitably limited by fabricating with single heat source.

In this study, the 800 W-600A sample and the 1000 W-300A sample are notable for their microstructure. The characteristics of these two samples are compared in Table 3. The depth of melt pool of 1000 W-300A sample is larger than 800 W-600A due to the higher laser power. It means that the shapes of the melt pool are different during the melting and solidification processing under these two process parameters. The grain morphology and size of these two samples are almost identical, but the phases in β grain are very different respectively. This has been explained by thermal analysis before. It causes the hardness of these two samples to show significant difference. This novel result differ from the conclusion that higher input energy lead

to coarser grains and coarser phase which can be obtained from past researches about metal additive manufacturing with single heat source. This implies that the limitation of microstructure controlling in laser

Table 3

Characteristics of 1000 W-300A sample and 800 W-600A sample.

	1000 W-300A sample	800 W-600A sample
Depth of melt pool	0.69 mm	0.59 mm
Thickness of equiaxed zone	75 μ m	75 μ m
Width of columnar grain	130 μ m	135 μ m
Phase	α'	$\alpha + \alpha'$
Hardness	415Hv	368.3Hv

additive manufacturing can be broken through by introducing a synchronous induction heat source.

The calculated microstructure formation conditions shown in Figs. 11, 12 and 13(b) and (d) indicate that the solidification conditions are extremely similar and the phase transform conditions are different under these two process parameters. The result demonstrates the ability to control the grains and phase separately during deposition processing by adjusting the laser energy and induction energy in synchronous induction assisted laser depositing.

5. Conclusions

Ti-6Al-4 V alloy samples were deposited by synchronous induction assisted laser deposition, and the influences of laser and induction energy on the grain morphology and phase was investigated. The main conclusions from this study are as follows:

- (1) The influence of induction energy on grain morphology in deposited layer is similar with that of laser energy. With the increase of input energy, the temperature gradient in solidification process decreases significantly and hence both of the thickness of equiaxed grain zone and the width of columnar grains increase accordingly.
- (2) In prior β grains, α phase appeared when input current increase to 600A. The fraction of α phase increases and the fraction of martensite decreases with the increase of laser power. The size of martensite remained the same when the input current increases and decreases with the increasing laser power. The size of α phase reduced when laser power rise from 800 W to 1200 W.
- (3) The addition of inductive heat source makes a "stair" in the thermal behavior curve between T_{β} and M_S due to the post-heating effect in the synchronous induction assisted laser deposition process. The cooling rate decreased obviously with the increase of input current and increased with the increase of laser power. So α phase can be precipitated due to the presence of the "stair".
- (4) Novel microstructures that consist of similar β grain morphology but different phase in β grains can be obtained by synchronous induction assisted laser deposition, which is very distinctive from usual laser deposition process. This discovery indicates a great potential of microstructure control, the grains and the phase can be controlled separately by adjusting the laser parameters and induction parameters.

CRediT authorship contribution statement

Wei Fan: Conceptualization, Methodology, Investigation, Formal analysis, Writing - original draft. **Hua Tan:** Conceptualization, Supervision. **Xin Lin:** Writing - review & editing. **Weidong Huang:** Writing - review & editing.

Acknowledgements

This work was partially supported by the National Natural Science Foundation of China (Grant No.51475380) and the National Key Research and Development Program of China (No. 2018YFB1106302). Wei Fan and Hua Tan contributed equally to this work.

References

- [1] Dirk Herzog, Vanessa Seyda, Additive manufacturing of metals, *Acta Mater.* 117 (2016) 371–392, <https://doi.org/10.1016/j.actamat.2016.07.019>.
- [2] E. William, Frazier, metal additive manufacturing: a review, *J. Mater. Eng. Perform.* 23 (2014) 1917–1928, <https://doi.org/10.1007/s11665-014-0958-z>.
- [3] Zhaoyang Liu, Huan Qi, Effects of substrate crystallographic orientations on crystal growth and microstructure formation in laser powder deposition of nickel-based superalloy, *Acta Mater.* 87 (2015) 248–258, <https://doi.org/10.1016/j.actamat.2014.12.046>.
- [4] Shang Sui, Jing Chen, Ma Liang, et al., Microstructures and stress rupture properties of pulse laser repaired Inconel 718 superalloy after different heat treatments, *J. Alloys Compd.* 770 (2019) 125–135, <https://doi.org/10.1016/j.jallcom.2018.08.063>.
- [5] Y.Y. Zhu, X.J. Tian, J. Li, et al., The anisotropy of laser melting deposition additive manufacturing Ti-6.5Al-3.5Mo-1.5Cr-0.3Si titanium alloy, *Mater. Des.* 67 (2015) 538–542, <https://doi.org/10.1016/j.matdes.2014.11.001>.
- [6] Alexander E. Wilson-Heid, Zhuqing Wang, Brenna McCormac, Allison M. Beese, Quantitative relationship between anisotropic strain to failure and grain morphology in additively manufactured Ti-6Al-4V, *Mater. Sci. Eng. A* 706 (2017) 287–294, <https://doi.org/10.1016/j.msea.2017.09.017>.
- [7] Y.M. Ren, X. Lin, X. Fu, et al., Microstructure and deformation behavior of Ti-6Al-4V alloy by high-power laser solid forming, *Acta Mater.* 132 (2017) 82–95, <https://doi.org/10.1016/j.actamat.2017.04.026>.
- [8] Parisa Farahmand, Radovan Kovacevic, Laser cladding assisted with an induction heater (LCAIH) to Ni-60%WC coating, *J. Mater. Process. Technol.* 222 (2015) 244–258, <https://doi.org/10.1016/j.jmatprotect.2015.02.026>.
- [9] Yongjun Huang, Xiaoyan Zeng, Investigating on cracking behavior of Ni-based coating by laser-induction hybrid cladding, *Appl. Surf. Sci.* 256 (2010) 5985–5992, <https://doi.org/10.1016/j.apsusc.2010.03.106>.
- [10] Boris Rottwinkel, Christian Nolke, Laser cladding for crack repair of CMSX-4 single-crystalline turbine parts, *Lasers Manuf. Mater. Process.* 4 (2017) 13–23, <https://doi.org/10.1007/s40516-016-0033-8>.
- [11] F. Brückner, C. Leyens, Hybrid laser manufacturing, *Laser Addit. Manuf.* (2017) 79–97, <https://doi.org/10.1016/B978-0-08-100433-3.00003-8>.
- [12] Xipeng Tan, Yihong Kok, Wei Quan Toh, et al., Revealing martensitic transformation and α/β interface evolution in electron beam melting three-dimensional-printed Ti-6Al-4V, *Sci. Rep.* 6 (2016) 26039–26048, <https://doi.org/10.1038/srep26039>.
- [13] J. Yang, H. Yu, J. Yin, et al., Formation and control of martensite in Ti-6Al-4V alloy produced by selective laser melting, *Mater. Des.* 108 (2016) 308–318, <https://doi.org/10.1016/j.matdes.2016.06.117>.
- [14] C. Rabadia, Y.J. Liu, G.H. Gao, et al., High-strength β stabilized Ti-Nb-Fe-Cr alloys with large plasticity, *Mater. Sci. Eng. A* 732 (2018) 368–377, <https://doi.org/10.1016/j.msea.2018.07.31>.
- [15] P. Zhang, S.X. Li, Z.F. Zhang, General relationship between strength and hardness, *Mater. Sci. Eng. A* 529 (2011) 62–73, <https://doi.org/10.1016/j.msea.2011.08.061>.
- [16] U. Ramamurty, S. Jana, Y. Kawamura, K. Chattopadhyay, Hardness and plastic deformation in a bulk metallic glass, *Acta Mater.* 53 (2005) 705–717, <https://doi.org/10.1016/j.actamat.2004.10.023>.
- [17] D. Rosenthal, Mathematical theory of heat distribution during welding and cutting, *Weld. J. 20* (1941) (1941) 220–234.
- [18] A.J. Pinkerton, L. Li, The development of temperature fields and powder flow during laser direct metal deposition wall growth, *Proc. Inst. Mech. Eng. C J. Mech. Eng. Sci.* 218 (2004) 531–542, <https://doi.org/10.1243/095440604323052319>.
- [19] Zhiru Liu, *Metal Induction Heat Treatment*, Mechanical Industry Press, Beijing, China, 1985.18.
- [20] O. Perret, Ph. Naudy, M. Bizouard, Two experimental methods to understand key-hole formation in pulse Nd: YAG laser welding, *Proc. SPIE 3888* (2000) 778–787, <https://doi.org/10.1117/12.377091>.
- [21] Xuefei Lu, Xin Lin, et al., Finite element analysis and experimental validation of the thermomechanical behavior in laser solid forming of Ti-6Al-4V, *Addit. Manuf.* 21 (2018) 30–40, <https://doi.org/10.1016/j.addma.2018.02.003>.
- [22] Beth E. Carroll, Todd A. Palmer, Allison M. Beese, Anisotropic tensile behavior of Ti-6Al-4V components fabricated with directed energy deposition additive manufacturing, *Acta Mater.* 87 (2015) 309–320, <https://doi.org/10.1016/j.actamat.2014.12.054>.
- [23] J.D. Hunt, Steady state columnar and equiaxed growth of dendrites and eutectic, *Mater. Sci. Eng.* 65 (1984) 75–83, [https://doi.org/10.1016/0025-5416\(84\)90201-5](https://doi.org/10.1016/0025-5416(84)90201-5).
- [24] W. Kurz, D.J. Fisher, Dendrite growth at the limit of stability: tip radius and spacing, *Acta Metall.* 29 (1981) 11–20, [https://doi.org/10.1016/0001-6160\(81\)90082-1](https://doi.org/10.1016/0001-6160(81)90082-1).
- [25] P.A. Kobry, S.L. Semiatin, Microstructure and texture evolution during solidification processing of Ti-6Al-4V, *J. Mater. Process. Technol.* 135 (2003) 330–339, [https://doi.org/10.1016/S0924-0136\(02\)00865-8](https://doi.org/10.1016/S0924-0136(02)00865-8).
- [26] J.D. Hunt, *Solidification and Casting of Metals*, 3, The Metals of Society, London, 1979.
- [27] T. Ahmed, H.J. Rack, Phase transformations during in $\alpha + \beta$ titanium alloys, *Mater. Sci. Eng. A* 243 (1998) 206–211, [https://doi.org/10.1016/S0921-5093\(97\)00802-2](https://doi.org/10.1016/S0921-5093(97)00802-2).
- [28] Frederick Lia, Z. Joshua, et al., Thermal and microstructure analysis of laser-based directed energy deposition for Ti-6Al-4V and Inconel 625 deposits, *Mater. Sci. Eng. A* 719 (2018) 1–10, <https://doi.org/10.1016/j.msea.2018.01.060>.
- [29] Xinhua Wu, Jing Liang, et al., Microstructure of laser-deposited Ti-6Al-4V, *Mater. Des.* 25 (2004) 137–144, <https://doi.org/10.1016/j.matdes.2003.09.009>.